Check for updates

ChemCatChem

Research Article
doi.org/10.1002/cctc.202401691

Chemistry Europe
European Chemical
Societies Publishing

www.chemcatchem.org

Photosynthetic Biomimetic System: Nickel Phthalocyanine and Biomass-Derived Carbon Quantum Dots for Enhanced Water Oxidation

Gabriel C. da Fonseca,[a, b, c] Fhysmélia F. de Albuquerque,[b] Rafael N. P. Colombo,[b] Rodrigo M. Iost,[b] Frank N. Crespilho,[b] and João C. P. de Souza*[d]

Efficient water oxidation is a crucial challenge for artificial photosynthesis and solar energy conversion. Here, we introduce a biomimetic photosynthetic system that combines Nickel(II) phthalocyanine-tetrasulfonic acid (NiPc) with carbon quantum dots (CQDs) derived from sugarcane biomass to enhance photoelectrochemical water oxidation. The CQDs effectively absorb UV and visible light, aiding electron transfer to NiPc, which significantly boosts photocurrent generation and reduces the overpotential. Electrochemical tests, including cyclic voltammetry and chronoamperometry under UV and blue light, show that the NiPc/CQD hybrid system delivers a notable increase in photocurrent density and stability compared to bare NiPc electrodes. By a membrane-free Clark-type electrode, molecular oxygen generated during photoelectrochemical water oxidation was detected. This sustainable system underscores the potential of biomass-derived CQDs as efficient, low-cost nanomaterials for solar-driven water oxidation, advancing renewable energy technologies.

Achieving efficient water oxidation at low overpotentials remains a significant challenge, particularly in the design of scalable and practical systems for solar energy conversion. Transition metal complexes, such as nickel phthalocyanine (NiPc), have emerged as promising catalysts due to their tunable redox properties and structural adaptability.[1–3] The central nickel ion in NiPc can undergo multiple oxidation states, allowing for fine control over its redox potential, which is essential for catalytic applications.[4] Additionally, the electronic environment of the metal center can be further optimized by modifying peripheral ligands or axial coordination, enabling enhanced catalytic activity and stability in various electrochemical processes.[3–5]

Despite these advantages, NiPc typically requires high overpotentials to efficiently drive the water oxidation reaction, which limits its broader application in artificial photosynthesis. Integrating nanomaterials that exhibit superior electron transfer and light-harvesting properties is a promising strategy to address this limitation.[2,6] Such materials can enhance the overall efficiency of the catalyst by facilitating charge separation and minimizing energy losses. One such material is carbon quantum dots (CQDs), which have garnered significant attention due to their remarkable optical and electronic properties.[1,2,7] In this study, we utilize CQDs derived from sugarcane biomass, an abundant carbon source, offering a sustainable route for nanomaterial production.[8,9] These CQDs exhibit strong light absorption over a broad range of wavelengths, including the visible spectrum (400–700 nm), making them ideal candidates for coupling with photocatalysts.[10,11] Specifically, CQDs possess high quantum yields, excellent photostability, and the ability to act as efficient electron donors when absorbing light. Their absorption also extends into the UV region (<400 nm), further enhancing their ability to capture and utilize solar energy in photocatalytic systems effectively.[12–15] It is known that the incorporation of molecular metal structures can improve the photoelectrochemical response in hybrid systems with CQDs.[16]

In this work, we demonstrate that the combination of NiPc and biomass-derived CQDs results in a remarkable enhancement in water oxidation under blue and UV irradiation. CQDs absorb light efficiently across the UV and visible ranges and facilitate energy transfer to the NiPc catalyst, promoting more efficient charge separation and electron transfer. This leads to significantly increased catalytic activity and lowers the overpotential required for water oxidation. The energy transfer process between CQDs and NiPc is crucial for enhanced performance, as it boosts electron mobility and optimizes the interaction

---

[a] G. C. da Fonseca
Goiano Federal Institute of Education, Science and Technology, Campus Rio Verde, Rio Verde, Goiás 75901–970, Brazil

[b] G. C. da Fonseca, F. F. de Albuquerque, R. N. P. Colombo, R. M. Iost, F. N. Crespilho
São Carlos Institute of Chemistry, University of São Paulo, São Carlos, São Paulo 13560–970, Brazil

[c] G. C. da Fonseca
BCMaterials, Basque Center for Materials, Applications and Nanostructures, UPV/EHU Science Park, Leioa 48940, Spain

[d] J. C. P. de Souza
Department of Chemistry, Faculty of Sciences, São Paulo State University, Bauru, São Paulo 17033–360, Brazil
E-mail: joao.perbone@unesp.br

Supporting information for this article is available on the WWW under https://doi.org/10.1002/cctc.202401691

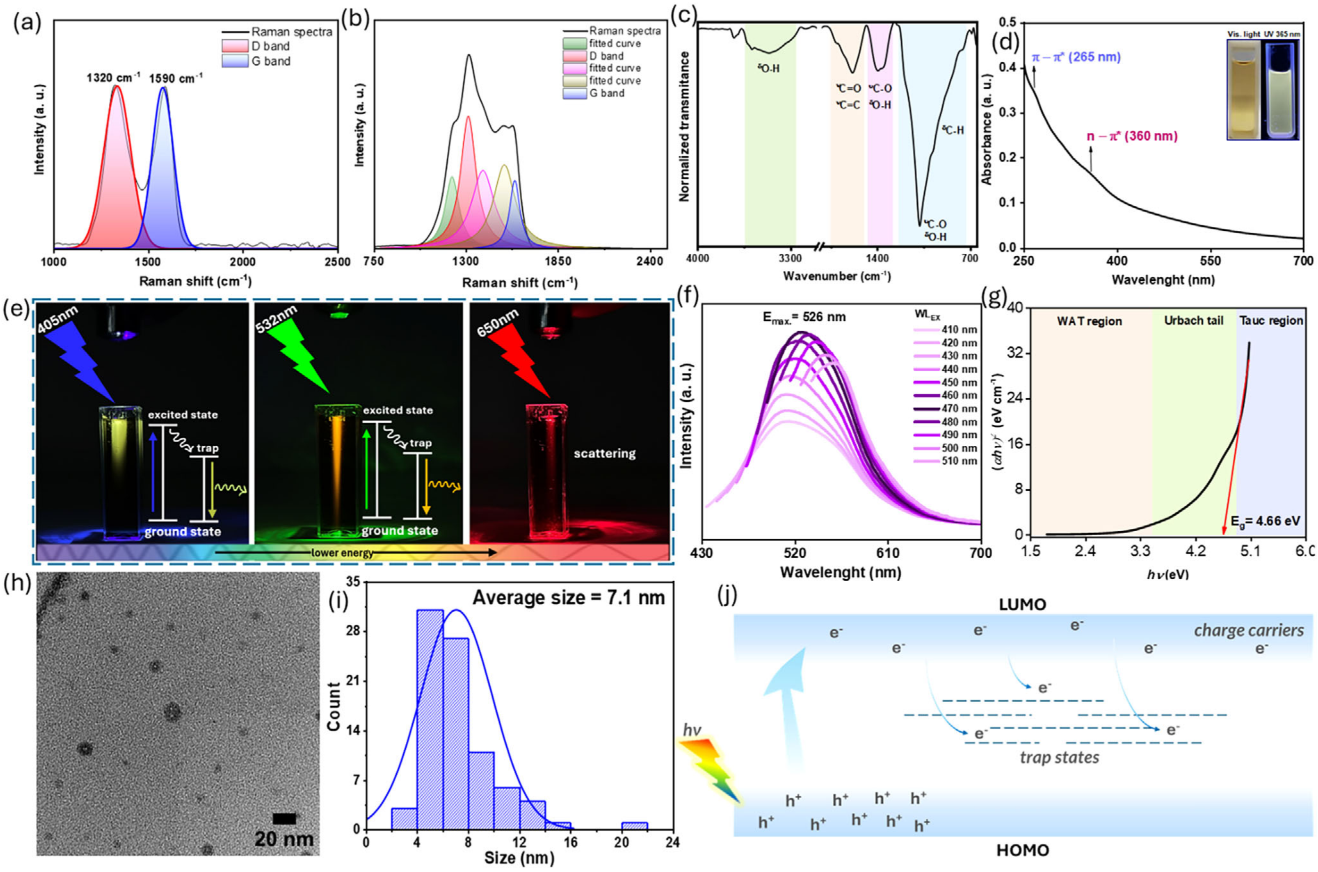

Figure 1. a) Raman spectra of pyrolyzed material presenting D and G bands. b) Raman spectra of CQDs. In this one, bands (green, magenta, and brown) other than D and G appear due to increased surface defects. c) FTIR spectra of CQDs. The assignments reveal the constitution of oxygen-containing functional groups. d) UV–vis absorption spectra of the carbon quantum dot suspension in water. Inset: photographs of the CQDs suspension under visible and 365 nm UV light. The π–π^* absorption band arises from band-to-band transitions of the sp^2 carbon. The n–π^* band is associated with the sub-band states from COOH and C═O edge groups. e) Mechanism for fluorescence emission induced by a laser pointer. Excitation in certain wavelengths leads to emission at longer wavelengths, the redshift. This mechanism attributes the phenomenon to traps in the CQD structure due to surface defects and functional groups. f) The emission spectrum shows the dependence on the excitation wavelength. Excitation wavelength varied from 410 to 510 nm, and the maximum emission intensity was observed at 526 nm upon excitation at 470 nm. The arrow indicates the increase in excitation wavelength. g) Tauc plot obtained from UV–vis data showing the dependence of $(\alpha h\nu)^2$ on the $(h\nu)$, by which we can determine the bandgap value (E_g). h) TEM image of CQDs. i) Size distribution with the average size of 7.1 nm, obtained by counting 84 particles from different regions of images from the same sample. j) Schematic representation of the mechanism for photogeneration of electron-hole pairs as charge carriers. The structural defects can act as traps for the recombination of electron-hole pairs.

between the light-absorbing quantum dots and the catalytic sites of NiPc. Our findings underscore the role of biomass-derived CQDs in advancing sustainable photocatalysis, demonstrating their capacity to reduce the energy input required for catalytic reactions while improving overall efficiency. This hybrid system, which combines the light-harvesting properties of CQDs with the catalytic potential of NiPc, represents a significant advancement in developing bio-inspired systems for solar fuel production.

A detailed experimental section is provided in the Supporting Information. Raman spectra of the pyrolyzed material to produce CDQs exhibited characteristic D and G bands at 1320 and 1590 cm^{-1}, respectively, indicating the presence of defects in the carbon structure, with an I_D/I_G ratio of 1.00 (Figure 1a). This defect density increased after the acid treatment was used to synthesize the CQDs (Figure 1b), with the I_D/I_G ratio rising to 1.97, suggesting a significant increase in surface defects and functionalization with oxygen-containing groups, such as carbonyl and hydroxyl, as confirmed by FTIR (Figure 1c). These functional groups enhance CQDs' solubility and electrostatic stability, essential for efficient photoelectrocatalysis. UV–vis spectroscopy revealed strong absorption bands at 265 nm (π–π^* transitions) and 360 nm (n–π^* transitions), indicating the presence of sp^2 carbon and oxygen heteroatoms (Figure 1d). The CQDs exhibited wavelength-dependent fluorescence, with maximum emission at 526 nm when excited at 470 nm (Figure 1f), attributed to surface defects acting as electron-hole traps (Figure 1j). The calculated bandgap of 4.66 eV correlates with the UV absorption data (Figure 1g). TEM images of the CQDs confirmed an average size of 7.1 nm (Figure 1h,i), and the zeta potential measurement of −22.6 mV indicated good suspension stability. Considering the results obtained from FTIR, the surface of the CQDs is decorated with various functional groups, which favors the origination of different surface defects, a result also shown by Raman spectroscopy; these are likely the source of multiple light emission centers within the structure of CQDs.[17]

The recombination of electron-hole pairs in the localized π and π^* electronic levels of the sp^2 sites can also explain the fluorescence; in such a manner, sp^2 sites remain within the σ and σ^* states of the sp^3 structure, thus resulting in weak absorption around UV–vis region but high emissions in the visible region.[18] The mechanism follows the excitation-dependent fluorescence emission to the size distribution and emissive traps onto the surface of carbon dots obtained from sugarcane molasses.[19] By irradiating the suspension with a blue laser, we can observe the redshift, emitting around the green region (Figure 1e). Furthermore, when irradiated with a green laser, the suspension emits light around the yellow/orange region. However, when irradiated with red light, the suspension only scatters it, revealing that it does not absorb light with longer wavelengths. As observed by fluorescence spectroscopy and laser pointer-induced fluorescence, a red shift phenomenon occurs in emissions. Functional groups and surface defects can introduce trap states in the band gap, where the photoexcited exciton can be trapped. The recombination of the electron-hole pair leads to the emission of photons with lower energy (longer wavelengths).[20,21] Herewith, we do not attribute the red shift of fluorescence to one feature, such as conjugated π-domains, surface defects, or size effects. But, considering the FTIR results, showing several oxygen-containing functional groups created by surface oxidation, an interpretation also sustained through Raman results, we conclude that a mechanism for this phenomenon might be associated with surface-state-related fluorescence. The performance of the CQDs in photoelectrochemical water oxidation was evaluated by assembling working electrodes with NiPc and CQDs on ITO substrates. The membrane-free Clark-type electrode was used to detect molecular oxygen generated during photoelectrochemical water oxidation (Figures S23 and S24).[22,23] As expected, the sensor registered an increase in the formation of O_2 at the photoanode after illumination. This confirms that the system operates effectively. AFM and XPS analyses were performed to explain the formation of layers and bilayers further (Figures S8–S14). In summary, the AFM supports the formation of layers in each step of the procedure and further highlights the role of a specific order of the film preparation. Cyclic voltammetry (CV) and chronoamperometry measurements were performed in both acidic ($pH = 1.0$) and basic ($pH = 9.6$) conditions under dark, UV (365 nm), and blue (405 nm) light irradiation. The NiPc/CQD electrode showed a notable enhancement in photocurrent density compared to the bare NiPc electrode (Figure 2). In acidic conditions (pH 1.0), under UV irradiation, the photocurrent reached 3.83 $\mu A\ cm^{-2}$ at 1.23 V versus RHE, which is 6.5 times higher than that of bare ITO and 1.9 times higher than the electrode with CQDs alone (Figure 3).

This increase in photocurrent is attributed to the effective generation and separation of electron-hole pairs in the CQDs, which then transfer electrons to NiPc, facilitating water oxidation. The increase in photocurrent density under UV light compared to blue light indicates that more energetic UV photons generate more electron-hole pairs. Electrochemical impedance spectroscopy (EIS) further supports this enhanced photocurrent, which revealed that integrating CQDs with NiPc reduces charge recombination at the electrode surface, allowing more efficient electron transfer and, consequently, a more effective water oxidation reaction. The chronoamperometry experiments further demonstrated the stability of the NiPc/CQD electrodes under prolonged light irradiation (Figure 3). The photocurrent remained stable throughout several on/off cycles of light exposure, suggesting that the photoelectrode assembly is robust. Interestingly, under UV light, the photocurrent continued to increase steadily during oxidation, whereas under blue light, it stabilized more quickly. This behavior can be attributed to the higher energy UV photons inducing a greater number of photogenerated carriers, which in turn sustain higher rates of water oxidation. The mechanism for the enhanced photoelectrocatalytic performance of NiPc/CQD electrodes involves the generation of electron-hole pairs in the CQDs upon light excitation. The photogenerated electrons are transferred from CQDs to the NiPc, facilitating water oxidation. In contrast, redox species in the CQDs consume the holes in the electrolyte, maintaining the charge balance. This process results in efficient water oxidation with reduced overpotential compared to bare NiPc electrodes. The enhanced separation of charge carriers and the efficient electron transfer facilitated by CQDs are key to the improved photocurrent response. Furthermore, integrating CQDs with NiPc forms a p–n junction, which helps create an internal electric field that promotes better charge separation. This feature is crucial for suppressing charge recombination, one of the primary factors that limit the efficiency of photoelectrocatalytic systems. The p-n junction enhances the charge carrier collection, improving overall water oxidation efficiency. In alkaline conditions ($pH = 9.6$), the CQD electrodes showed significant photocurrent even in the dark, suggesting that the graphitic nature of the CQDs enhances the conductivity of the surface. However, under UV irradiation, the photocurrent for NiPc/CQDs at $pH = 9.6$ was higher than in acidic conditions, reaching up to 60 $\mu A\ cm^{-2}$ at 1.5 V versus RHE (Figure S18). This suggests that alkaline electrolytes may promote more efficient water oxidation due to better interaction between the CQDs and the electrolyte, potentially by facilitating proton transfer or influencing the ionic strength of the medium. Figure S18 also shows overlayed CVs for the assembled CQDs and NiPc before and after blue and UV irradiation to directly compare the impact of light on the photoelectrochemical response. Electrochemical impedance spectroscopy was carried out in HCl, pH 1.0, under dark and under blue and UV irradiation with an applied bias of 0 V versus OCP. Figure S19 presents the Nyquist plots and equivalent circuits, and Table S6 presents the parameters from fitting the EIS spectra for working electrodes with CQDs. In the equivalent circuit (RS{Q1[R1(R2C2)]}), R, C, and Q are resistance, capacitance, and constant phase element (CPE), respectively. CPE is characteristic of porous or rough materials, representing a frequency-dependent capacitance.[24] The assembly of CQDs and NiPc onto the ITO results in a heterogeneous surface with non-uniform current distribution; by that, the capacitance of porous materials is represented by a CPE, dependent on Y02 and n ($0 \leq n \leq 1$); for ideal capacitors, $n = 1$. The capacitance values for Q_1 and C_2 increased for measurements under irradiation, as seen in Table S6, which was expected since, at open circuit conditions, a charge accumulation arises at the electrode/electrolyte interface.[24] From the

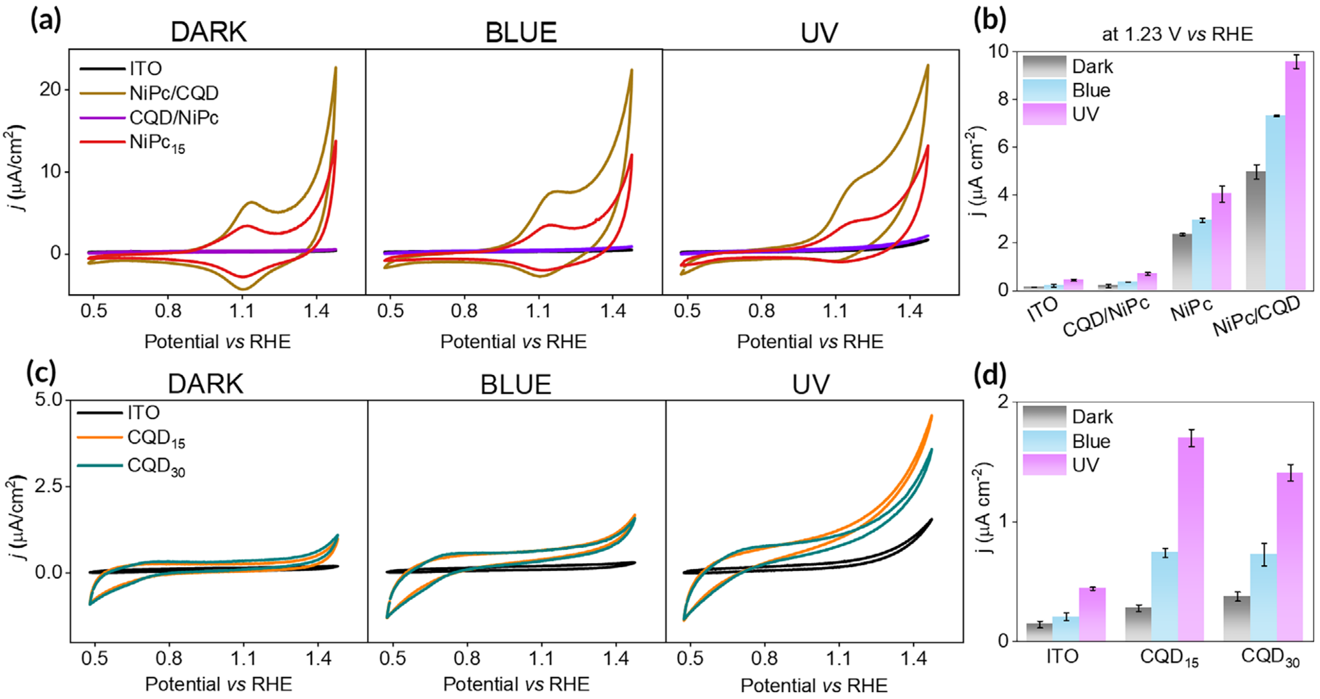

Figure 2. a) Current–density profile of NiPc and CQD electrodes at dark and under blue and UV irradiation. b) The maximum current density at 1.23 V versus RHE shows the increase under irradiation. NiPc/QCD electrode shows a higher rate of charge transfer. c) Current–density profile of CQD electrodes at dark and under blue and UV irradiation. d) The maximum current–density at 1.23 V versus RHE for CQD electrodes.

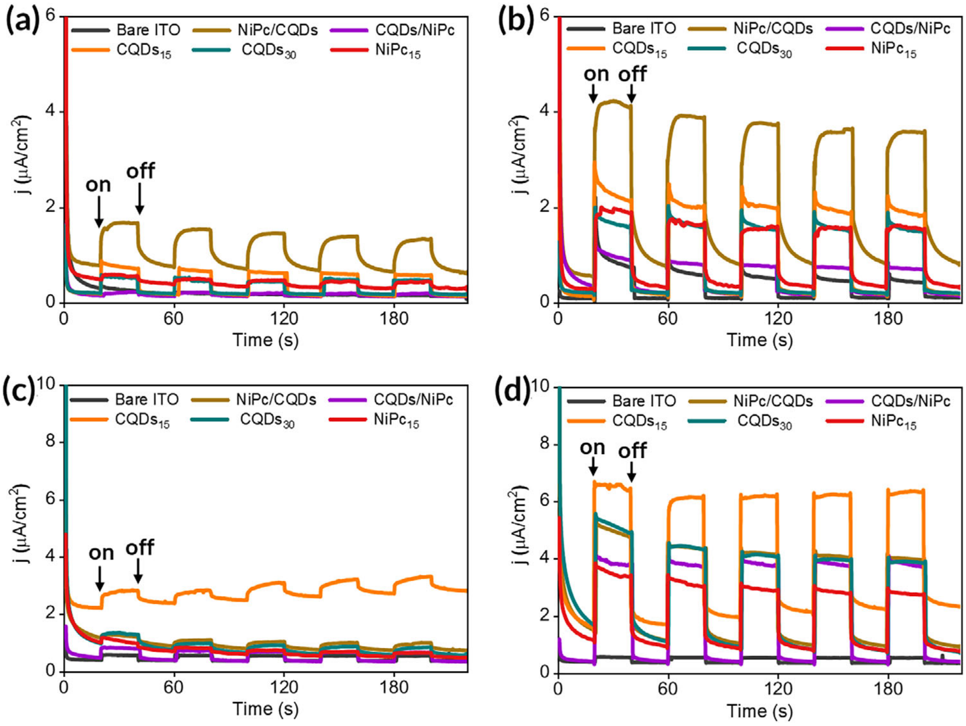

Figure 3. Chronoamperometry profiles of LbL assembled electrodes with NiPc and/or CQDs with the applied bias of 1.0 V. a) Analysis in HCl pH = 1.0 and blue light. b) Analysis in HCl pH = 1.0 and UV light. c) Analysis in carbonate/bicarbonate buffer pH = 9.6 and blue light. d) Analysis in carbonate/bicarbonate buffer pH = 9.6 and UV light. Note: The legend concerns all experimental data. "ON" and "OFF" mean turning the light source ON and OFF the light source. The net increase in current density for all experiments is compared to the photocurrent of the bare ITO.

EIS performed in the dark, the intrinsic electronic properties of the electrodes were investigated through the Mott–Schottky (M–S) plots (1 kHz). Figure S20 shows the M–S plots, and Table S6 shows the flat band potential (VFB) obtained from the extrapolation to the *x*-intercept. Also, the number of donors (ND) was calculated from Equation S2. All M–S plots present positive slopes, indicating that they are n-type semiconductors, with electrons as the majority carriers. The formation of a p–n interface induces an electric field within the space charge region, leading to a higher hole accumulation at the electrode surface. This improvement in charge carrier collection could lead to improved photoelectrochemical water oxidation due to the higher number of holes on the electrode surface.[25] The VFB values of all electrodes were lower than the bare ITO; this negative shift strengthens the band bending at the electrode/electrolyte interface and can also indicate a decrease in charge recombination and reduction of the overpotential for water oxidation.[26] The open circuit potential (OCP) measured before EIS analysis under dark and light irradiation was combined in Figure S21. First, we should note that electrodes with CQDs in direct contact with ITO have similar OCP values, which shift to negative potentials under blue and UV light. Meanwhile, for NiPc/CQDs electrodes, the potential shifts to more positive ones under UV and blue irradiation, while the NiPc electrode shifts to a more negative potential under UV light. One can note that electrodes with CQDs have larger ΔOCP, showing higher photovoltages. This indicates an increased band bending at the CQD/electrolyte interface.[27]

The photoelectrochemical performance of five working electrodes assembled with NiPc and/or CQDs was presented here. The photocurrent density observed for the CQD_{15} electrode under blue and UV irradiation shows the effect of photogeneration of electron-hole pairs (Figure 1j). The photogenerated electrons increase the charge transfer over the circuit; by that, the holes in the valence band of CQDs can react with water to generate oxygen, and the electrons flow to the counter electrode where a reduction reaction can occur. Furthermore, the assembly of CQDs over NiPc onto ITO can increase even more the photocurrent. In the same way, the photogenerated electron holes interact with NiPc, which also presents a photocurrent itself. The photogenerated holes in the valence band of NiPc can transfer to the LUMO of CQDs and then oxidize water to oxygen (Figure S22). Simultaneously, the photogenerated electrons can transfer from CQDs to NiPc and then to the external circuit for reduction reactions in the counter electrode, resulting in higher measured photocurrent density

In summary, the combination of biomass-derived CQDs with NiPc results in a significant enhancement in photoelectrochemical water oxidation. The CQDs, synthesized from sugarcane bagasse, act as effective light harvesters and charge carriers, facilitating the separation of electron-hole pairs and improving the photocurrent response of NiPc electrodes. The stability and enhanced performance of the NiPc/CQD electrodes under UV and blue light irradiation highlight the potential of this hybrid system for solar-driven water oxidation. This work demonstrates the viability of CQDs as low-cost, sustainable nanomaterials for advanced photoelectrocatalytic applications.

Acknowledgments

To the Goiano Federal Institute of Science, Education and Technology, and São Carlos Institute of Chemistry, USP, for the facilities and infrastructure needed to perform this work. To FAPESP for financial support to acquire reactants. To CAPES for financial support (G. C. F. scholarship process number 88887.892512/2023–00). FAPESP 2021/05665–7 (R.N.P.C.), 2018/22214–6, 2022/09164–5, 2022/06563-6, 2020/12404-2 and 2023/01529–7 (F.N.C.). The authors acknowledge KherveFitting open-source software by G. Kerherve for XPS analysis. The authors thank Graziela Cristina Sedenho for the support. F.F.A. acknowledges support from FAPESP (Grant 2023/17020–6 and 2025/05509-6).

The Article Processing Charge for the publication of this research was funded by the coordenação de Aperfeiçoamento de Pessoal de Nível Superior - Brasil (CAPES) (ROR identifier: 00x0ma614).

Conflict of Interests

The authors declare no conflict of interest.

Data Availability Statement

The data that support the findings of this study are available from the corresponding author upon reasonable request.

Supporting Information

The authors have cited additional references within the Supporting Information.[28–43]

Keywords: Carbon quantum dots · Photoelectrocatalysis · Water oxidation reaction

[1] S. Xu, W. Sun, X. Meng, Y. Dong, Y. Ding, *J. Phys. Chem. C* **2021**, *125*, 24413–24421.
[2] A. Kolay, P. Ghosal, M. Deepa, *ACS Sustainable Chem. Eng.* **2020**, *8*, 8593–8603.
[3] S. A. Mirshokraee, M. Muhyuddin, N. Pianta, E. Berretti, L. Capozzoli, J. Orsilli, F. D'Acapito, R. Viscardi, A. Cosenza, P. Atanassov, C. Santoro, A. Lavacchi, *ACS Catal.* **2024**, *14*, 14524–14538.
[4] W. S. Alencar, F. N. Crespilho, M. V. A. Martins, V. Zucolotto, O. N. Oliveira Jr, W. C. Silva, *Phys. Chem. Chem. Phys.* **2009**, *11*, 5086.
[5] M. K. Barman, B. Jana, S. Bhattacharyya, A. Patra, *J. Phys. Chem. C.* **2014**, *118*, 20034–20041.
[6] J. Feng, J. Bian, L. Bai, S. Xi, Y. Wang, C. Chen, L. Jing, *Appl. Catal. B Environ.* **2021**, *295*, 120260.
[7] X. Miao, P. Zhang, B. Wang, X. Bai, W. Liu, *Appl. Catal. B Environ.* **2024**, *357*, 124268.
[8] D. K. Patel, S.o-Y. Won, E. Jung, S. Deb Dutta, T. V. Patil, K.i-T. Lim, S. Soo Han, *Mater. Lett.* **2024**, *361*, 136152.
[9] X. W. Fang, H. Chang, T. Wu, C. H. Yeh, F. L. Hsiao, T. S. Ko, C. L. Hsieh, M. Y. Wu, Y. W. Lin, *ACS Omega* **2024**, *9*, 23573–23583.
[10] S. Khojiev, G. Hojiyeva, O. Tursunkulov, D. Chen, H. S. H. Mohamed, A. Kholikov, K. Akbarov, J. Liu, Y.u Li, *ACS Appl. Nano Mater.* **2023**, *6*, 14669–14679.

[11] S. Bhattacharyya, F. Ehrat, P. Urban, R. Teves, R. Wyrwich, M. Döblinger, J. Feldmann, A. S. Urban, J. K. Stolarczyk, *Nat. Commun.* **2017**, *8*, 1–9.
[12] H. Y. Wang, R. Hu, N. Wang, G. L. Hu, K. Wang, W. H. Xie, R. Cao, *Appl. Catal. B Environ.* **2021**, *296*, 120378.
[13] H. Luo, S. Dimitrov, M. Daboczi, J. S. Kim, Q. Guo, Y. Fang, M. A. Stoeckel, P. Samorì, O. Fenwick, A. B. Jorge Sobrido, X. Wang, M. M. Titirici, *ACS Appl. Nano Mater.* **2020**, *3*, 3371–3381.
[14] X. Chen, X. Zhang, H. Wang, H. Guo, W. Cui, *J. Mater. Sci.* **2024**, *59*, 17846–17859.
[15] J. Xu, H. Olvera-Vargas, G. H. X. Ou, H. Randriamahazaka, O. Lefebvre, *Chemosphere* **2023**, *341*, 140077.
[16] B. C. M. Martindale, G. A. M. Hutton, C. A. Caputo, E. Reisner, *J. Am. Chem. Soc.* **2015**, *137*, 6018–6025.
[17] Z. Wu, X. Liu, H. Li, Z. Sun, M. Cao, Z. Li, C. Fang, J. Zhou, C. Cao, J. Dong, S. Zhao, Z. Chen, *Nat. Commun.* **2023**, *14*, 1–9.
[18] H. Ding, X. H. Li, X. B. Chen, J. S. Wei, X. B. Li, H. M. Xiong, *J. Appl. Phys.* **2020**, *127*, 231101.
[19] G. Huang, X. Chen, C. Wang, H. Zheng, Z. Huang, D. Chen, H. Xie, *RSC Adv.* **2017**, *7*, 47840–47847.
[20] L. Tang, R. Ji, X. Cao, J. Lin, H. Jiang, X. Li, K. S. Teng, C. M. Luk, S. Zeng, J. Hao, S. P. Lau, *ACS Nano* **2012**, *6*, 5102–5110.
[21] A. Cayuela, M. L. Soriano, C. Carrillo-Carrión, M. Valcárcel, *Chem. Commun.* **2016**, *52*, 1311–1326.
[22] G. C. Sedenho, S. Q. Nascimento, M. Zamani, F. N. Crespilho, A. L. Furst, *Adv. Sci.* **2024**, *11*, 2402234.
[23] C. C. L. McCrory, S. Jung, J. C. Peters, T. F. Jaramillo, *J. Am. Chem. Soc.* **2013**, *135*, 16977–16987.
[24] K. Ranganathan, A. Morais, I. Nongwe, C. Longo, A. F. Nogueira, N. J. Coville, *J. Mol. Catal. A Chem.* **2016**, *422*, 165–174.
[25] H. Lim, J. Y. Kim, E. J. Evans, A. Rai, J. H. Kim, B. R. Wygant, C. B. Mullins, *ACS Appl. Mater. Interfaces* **2017**, *9*, 30654–30661.
[26] W. Kong, X. Zhang, S. Liu, Y. Zhou, B. Chang, S. Zhang, H. Fan, B. Yang, *Adv. Mater. Interfaces* **2019**, *6*, 1801653.
[27] R. Chong, Z. Wang, J. Lv, J. Rong, L. Zhang, Y. Jia, L. Wang, Z. Chang, X. Wang, *J. Catal.* **2021**, *399*, 170–181.
[28] J. Klein, L. Kampermann, B. Mockenhaupt, M. Behrens, J. Strunk, G. Bacher, *Adv. Funct. Mater.* **2023**, *33*, 1–19.
[29] S. Jing, Y. Zhao, R. C. Sun, L. Zhong, X. Peng, *ACS Sustainable Chem. Eng.* **2019**, *7*, 7833–7843.
[30] M. Xue, Z. Zhan, M. Zou, L. Zhang, S. Zhao, *New J. Chem.* **2016**, *40*, 1698–1703.
[31] Y. Liu, N. Xiao, N. Gong, H. Wang, X. Shi, W. Gu, L. Ye, *Carbon N. Y.* **2014**, *68*, 258–264.
[32] S. Pandiyan, L. Arumugam, S. P. Srirengan, R. Pitchan, P. Sevugan, K. Kannan, G. Pitchan, T. A. Hegde, V. Gandhirajan, *ACS Omega* **2020**, *5*, 30363–30372.
[33] F. Wu, H. Su, X. Zhu, K. Wang, Z. Zhang, W. K. Wong, *J. Mater. Chem. B* **2016**, *4*, 6366–6372.
[34] A. Abbas, T. A. Tabish, S. J. Bull, T. M. Lim, A. N. Phan, *Sci. Rep.* **2020**, *10*, 1–16.
[35] F. Aldakhil, N. A. Alarfaj, S. A. Al-Tamimi, M. F. El-Tohamy, *R. S. C. Adv.* **2024**, *14*, 19969–19982.
[36] Q. Chen, G. Lin, L. Meng, L. Zhou, L. Hu, J. Nong, Y. Li, J. Wang, K. Hu, Q. Yu, *Chem. Phys. Lett.* **2020**, *749*, 137428.
[37] Q. Gao, X. Guo, L. Meng, M. Liu, L. Chen, H. Li, J. Hu, *Int. J. Biol. Macromol.* **2023**, *253*, 126332.
[38] G. G. Ninan, M. Varghese, M. Balachandran, *Opt. Mater. (Amst).* **2024**, *154*, 115730.
[39] A. Abbas, S. Rubab, A. Rehman, S. Irfan, H. M. A. Sharif, Q. Liang, T. A. Tabish, *Mater. Today Chem.* **2023**, *30*, 101555.
[40] V. Zucolotto, M. Ferreira, **2003**.
[41] L. N. Furini, C. S. Martin, S. A. Camacho, R. J. G. Rubira, J. D. Fernandes, E. A. Silva, T. C. Gomes, G. M. Stunges, C. J. L. Constantino, P. Alessio, *Thin Solid Films* **2020**, *699*, 137897.
[42] C. S. Martin, H. S. Kavazoi, C. M. Miyazaki, P. Alessio, C. J. L. Constantino, *Chemosensors* **2023**, *11*, 372.
[43] K. Gelderman, L. Lee, S. W. Donne, *J. Chem. Educ.* **2007**, *84*, 685.

Manuscript received: October 2, 2024
Revised manuscript received: July 29, 2025
Accepted manuscript online: August 1, 2025
Version of record online: ■■, ■■